The Distribution of Radioactive 44ti In Cassiopeia A

Grefenstette, Brian W.; Fryer, Chris L.; Harrison, Fiona A.; Boggs, Steven E.; DeLaney, Tracey; Laming, J. Martin; Reynolds, Stephen P.; Alexander, David M.; Barret, Didier; Christensen, Finn Erland

Total number of authors:
31

Link back to DTU Orbit

THE DISTRIBUTION OF RADIOACTIVE ^{44}Ti IN CASSIOPEIA A

BRIAN W. GREFENSTETTE[1], CHRIS L. FRYER[2], FIONA A. HARRISON[1], STEVEN E. BOGGS[3], TRACEY DELANEY[4], J. MARTIN LAMING[5], STEPHEN P. REYNOLDS[6], DAVID M. ALEXANDER[7], DIDIER BARRET[8], FINN E. CHRISTENSEN[9], WILLIAM W. CRAIG[3,10], KARL FORSTER[1], PAOLO GIOMMI[11], CHARLES J. HAILEY[12], ALAN HORNSTRUP[9], TAKAO KITAGUCHI[13], J. E. KOGLIN[14], LAURA LOPEZ[15], PETER H. MAO[1], KRISTIN K. MADSEN[1], HIROMASA MIYASAKA[1], KAYA MORI[12], MATTEO PERRI[11,16], MICHAEL J. PIVOVAROFF[10], SIMONETTA PUCCETTI[11,16], VIKRAM RANA[1], DANIEL STERN[17], NIELS J. WESTERGAARD[9], DANIEL R. WIK[18,19], WILLIAM W. ZHANG[19], AND ANDREAS ZOGLAUER[3]

[1] Cahill Center for Astrophysics, 1216 E. California Boulevard, California Institute of Technology, Pasadena, CA 91125, USA; bwgref@srl.caltech.edu
[2] CCS-2, Los Alamos National Laboratory, Los Alamos, NM 87545, USA
[3] Space Sciences Laboratory, University of California, Berkeley, CA 94720, USA
[4] Physics & Engineering Department, West Virginia Wesleyan College, Buckhannon, WV 26201, USA
[5] Space Science Division, Naval Research Laboratory, Code 7684, Washington, DC 20375, USA
[6] Physics Department, NC State University, Raleigh, NC 27695, USA
[7] Centre for Extragalactic Astronomy, Department of Physics, Durham University, Durham DH1 3LE, UK
[8] Université de Toulouse; UPS-OMP; IRAP; Toulouse, France & CNRS; Institut de Recherche en Astrophysique et Planétologie; 9 Avenue colonel Roche, BP 44346, F-31028 Toulouse cedex 4, France
[9] DTU Space—National Space Institute, Technical University of Denmark, Elektrovej 327, DK-2800 Lyngby, Denmark
[10] Lawrence Livermore National Laboratory, Livermore, CA 94550, USA
[11] ASI Science Data Center (ASDC), via del Politecnico, I-00133 Rome, Italy
[12] Columbia Astrophysics Laboratory, Columbia University, New York, NY 10027, USA
[13] Department of Physical Science, Hiroshima University, 1-3-1 Kagamiyama, Higashi-Hiroshima, Hiroshima 739-8526, Japan
[14] Kavli Institute for Particle Astrophysics and Cosmology, SLAC National Accelerator Laboratory, Menlo Park, CA 94025, USA
[15] Department of Astronomy and Center for Cosmology & Astro-Particle Physics, The Ohio State University, Columbus, OH 43210
[16] INAF—Astronomico di Roma, via di Frascati 33, I-00040 Monteporzio, Italy
[17] Jet Propulsion Laboratory, California Institute of Technology, 4800 Oak Grove Drive, Pasadena, CA 91109, USA
[18] Department of Physics and Astronomy, Johns Hopkins University, Baltimore, MD 21218, USA
[19] NASA Goddard Space Flight Center, Greenbelt, MD 20771, USA

ABSTRACT

The distribution of elements produced in the innermost layers of a supernova explosion is a key diagnostic for studying the collapse of massive stars. Here we present the results of a 2.4 Ms *NuSTAR* observing campaign aimed at studying the supernova remnant Cassiopeia A (Cas A). We perform spatially resolved spectroscopic analyses of the ^{44}Ti ejecta, which we use to determine the Doppler shift and thus the three-dimensional (3D) velocities of the ^{44}Ti ejecta. We find an initial ^{44}Ti mass of $(1.54 \pm 0.21) \times 10^{-4}\ M_{\odot}$, which has a present-day average momentum direction of $340° \pm 15°$ projected onto the plane of the sky (measured clockwise from celestial north) and is tilted by $58° \pm 20°$ into the plane of the sky away from the observer, roughly opposite to the inferred direction of motion of the central compact object. We find some ^{44}Ti ejecta that are clearly interior to the reverse shock and some that are clearly exterior to it. Where we observe ^{44}Ti ejecta exterior to the reverse shock we also see shock-heated iron; however, there are regions where we see iron but do not observe ^{44}Ti. This suggests that the local conditions of the supernova shock during explosive nucleosynthesis varied enough to suppress the production of ^{44}Ti by at least a factor of two in some regions, even in regions that are assumed to be the result of processes like α-rich freezeout that should produce both iron and titanium.

Key words: gamma rays: general – ISM: supernova remnants – nuclear reactions, nucleosynthesis, abundances – X-rays: individual (Cassiopeia A)

Supporting material: animations

1. INTRODUCTION

Young supernova remnants (SNRs) are laboratories that we can use to study nucleosynthesis and the dynamics in supernova explosions. One key diagnostic in young remnants is the relative production of titanium, nickel, and silicon as observed through atomic transitions in the 0.1–10 keV band and, in the case of ^{44}Ti, through γ-rays emitted through radioactive decay.

The physical processes that produce these elements in core-collapse supernova explosions depend on the local conditions of the shock during explosive nucleosynthesis. The innermost ejecta in the supernova, the silicon layer, is shock-heated, fusing the silicon into nickel. However, due to Coulomb repulsion, it is unlikely that two ^{28}Si nuclei will fuse directly to ^{56}Ni. Instead, photodisintegration first rearranges the abundances, producing a set of clusters of nuclei with many reactions contributing to the final relic abundances.

The local supernova shock conditions can be parameterized by the peak temperature of the ejecta and the density of the ejecta at that temperature. Different regions of this parameter space correspond to different reactions dominating the nucleosynthesis (Magkotsios et al. 2010). An example of this is a region where incomplete silicon photodisintegration leads to partial silicon burning, leaving behind silicon-rich ejecta. Another is a region where a high density of free α-particles results in the "freezing out" of nuclear reactions (i.e., "α-rich freezeout," Woosley et al. 1973), which can lead to ejecta rich

with elements heavier than the iron group (e.g., Woosley & Hoffman 1992).

For a given supernova, the innermost ejecta have a wide range of peak temperatures and densities, and therefore a wide range of reactions can play a role in the nucleosynthetic yields. The ^{44}Ti yield is very sensitive to these conditions and thus is an ideal probe of nuclear and explosion physics. ^{56}Ni is much less sensitive to these conditions and instead is ideally suited to delineating the region where silicon burning occurs. Using the yields of both nickel and titanium, we can better identify the burning regions and their exact conditions.

The abundance of ^{56}Ni is measured by observing atomic transitions in shock-heated iron that are currently present in the SNR because iron is a decay product of ^{56}Ni. Determining the exact iron abundance from observations is not, however, straightforward because this requires models of the shock heating and the ionization state of the iron and, crucially, it requires a model of the density of the iron (e.g., Hwang & Laming 2012). In addition, some of the observed iron could be material swept up in the supernova shock rather than iron synthesized in the explosion. All these uncertainties make it difficult to determine the exact iron abundance and, therefore, the initial nickel abundance.

The abundance of ^{44}Ti is easier to determine since it is seen via the radioactive decays of ^{44}Ti $\rightarrow$ ^{44}Sc, producing a gamma-ray line at 1157 keV, and ^{44}Sc $\rightarrow$ ^{44}Ca, which produces a pair of gamma-ray lines at 78.32 and 67.87 keV. The branching ratios of the 1157, 78.32, and 67.87 keV lines are 99.9%, 96.4%, and 93%, respectively (Chen et al. 2011).[20] The present-day flux of photons produced in the radioactive decay of ^{44}Ti is therefore directly proportional to the initial synthesized mass of ^{44}Ti, independent of local conditions. For SNRs that are a few hundred years old, the ^{44}Ti, which has a half-life of 58.9 ± 0.3 yr (Ahmad et al. 2006), is still abundant enough to be observed.

Cassiopeia A (Cas A) is arguably the best-studied core-collapse SNR. It is young, with an explosion date inferred from the dynamical motion of the ejecta knots of 1671 (Thorstensen et al. 2001), and is relatively nearby at 3.4 kpc (Reed et al. 1995). ^{44}Ti has been detected in Cas A by the COMPTEL instrument on the *Compton Gamma-Ray Observatory (CGRO)* (Iyudin et al. 1994), *BeppoSAX* (Vink et al. 2001), the IBIS/ISGRI instrument on the *INTEGRAL* Observatory (Renaud et al. 2006), and *NuSTAR* (Grefenstette et al. 2014). Upper limits consistent with the detections were obtained using the OSSE instrument on *CGRO* (The et al. 1996), *RXTE* (Rothschild & Lingenfelter 2003), and the SPI instrument on *INTEGRAL* (Martin et al. 2009). A comparison of the total yield from all of these observations demonstrates that all measurements of the initial ^{44}Ti mass using the 68 and 78 keV lines are consistent with an initial ^{44}Ti mass of $(1.37 \pm 0.19) \times 10^{-4}$ $M_\odot$ (Siegert et al. 2015). However, only *NuSTAR* is capable of spatially resolving the remnant and has the energy resolution to search for Doppler broadening of the 67.87 and 78.32 keV decay lines of ^{44}Ti.

Our analysis of the initial *NuSTAR* observations demonstrated that the ^{44}Ti is highly asymmetric and does not trace the observed distribution of Fe K emission observed by *Chandra* (Grefenstette et al. 2014, and Figure 1). A highly collimated

axisymmetric jet engine had previously been invoked to explain the high ratio of ^{44}Ti/^{56}Ni in Cas A (e.g., Nagataki et al. 1998). However, the ^{44}Ti ejecta do not appear to be collimated in a jet-like structure associated with the NE/SW Si/Mg jet (e.g., the green layer in Figure 1) observed by *Chandra*, arguing that the Si/Mg asymmetric emission is not, in fact, indicative of a jet-driven explosion.

Unlike in SN1987A, where the ^{44}Ti decay lines appear to be redshifted but narrow (Boggs et al. 2015), in Cas A we found that the decay lines were measurably broadened, indicating that there is a diversity in the direction of motion of the ^{44}Ti ejecta. Our previous work using ~1 Ms of *NuSTAR* observations did not have sufficient statistical power to perform a spatially resolved spectroscopic analysis of the ^{44}Ti ejecta and so we were only able to describe the spatially integrated kinematics.

In this paper, we present an analysis of 2.4 Ms of *NuSTAR* observations. In Section 2 we describe the observations and the analysis techniques used to determine the three-dimensional (3D) spatial positions of the ^{44}Ti ejecta knots. In Section 3 we present our results, while in Section 4 we compare and contrast the properties of the ^{44}Ti with other known features of the remnant in the X-ray, infrared, and optical, and discuss the implications of these results in the context of theoretical models of the supernova explosion.

2. DATA AND METHODS

2.1. NuSTAR Data

NuSTAR is the first focusing, hard X-ray observatory. It is composed of two co-aligned X-ray telescopes (FPMA and FPMB) observing the sky in the energy range 3–79 keV (Harrison et al. 2013). The field of view of each *NuSTAR* telescope is roughly $12' \times 12'$ and has a point-spread function (PSF) with a FWHM of $18''$ and a half-power diameter of $58''$.

NuSTAR observed Cas A during the first 18 months of the *NuSTAR* mission (Table 1) with a total of 2.4 Ms of exposure time. These observations include the original ~1 Ms of data that we have presented previously (Grefenstette et al. 2014). We reduced the *NuSTAR* data with the *NuSTAR* Data Analysis Software (NuSTARDAS) version 1.4.1 and *NuSTAR* calibration database (CALDB) version 20150316 to produce images, exposure maps, and response files for each telescope.

We examined the background reports from the *NuSTAR* Science Operations Centerand identified solar flares during three sequence IDs (40021003003, 40021011002, and 40021015002). As the flux from the solar flares only affects the spectrum below 10 keV (Wik et al. 2014) and the amount of time that is affected by solar flares is small compared to the duration of the observations, we do not apply any filtering to the data. We do not use the data for sequence IDs 40021001004, 40021002010, and 40021003002 because these short observations were significantly offset from the target pointing position.

2.2. Data Reduction

We leverage the increased exposure time relative to our previous work to perform an analysis on smaller spatial scales, though at lower signal-to-noise ratio than when integrating over the remnant as a whole.

Figure 2 shows the 65–70 keV *NuSTAR* image of Cas A. To produce this image we combine all of the data (for all epochs and both telescopes) using `ximage` and then subtract the similarly combined background images. We smooth the result with an

---

[20] We note that our branching ratios are based on the most recent nuclear physics measurements and are subtly different than those reported in other papers on ^{44}Ti (e.g., Grebenev et al. 2012).
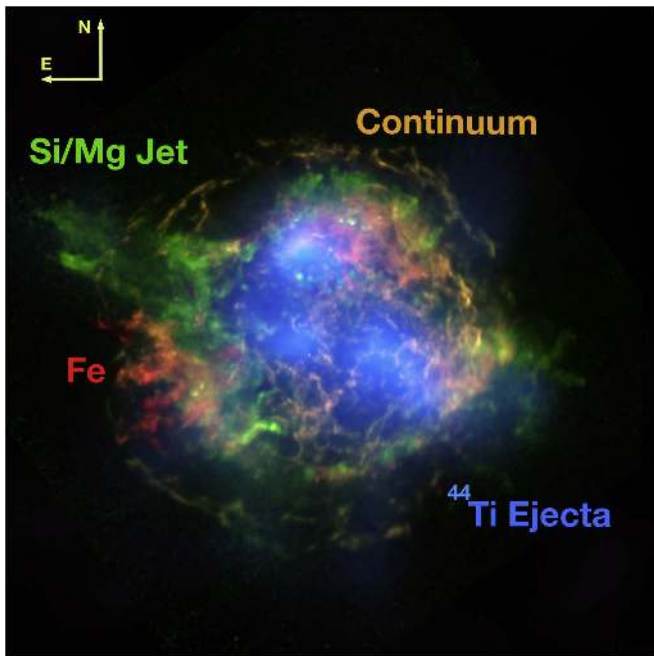
Figure 1. The spatial distribution of ^{44}Ti in Cas A compared with the other bright X-ray features. The *NuSTAR* 65–70 keV background-subtracted image covering the 68 keV ^{44}Sc line tracing the ^{44}Ti-rich ejecta is shown in blue. The *NuSTAR* image has been adaptively smoothed for clarity. The 4–6 keV continuum observed by *Chandra* is shown in gold, the ratio in the Si/Mg band highlighting the NE/SW jet is shown in green (data courtesy NASA/CXC, Si/Mg ratio image J. Vink), while the distribution of X-ray-emitting iron is shown in red (Fe distribution courtesy U. Hwang). Image credit: Robert Hurt, NASA/JPL-Caltech.

Table 1
NuSTAR Observations of Cas A

OBSID	Exposure	UT Start Date
40001019002	294 ks	2012 Aug 18
40021001002	190 ks	2012 Aug 27
40021001004[a]	29 ks	2012 Oct 07
40021001005	228 ks	2012 Oct 07
40021002002	288 ks	2012 Nov 23
40021002006	160 ks	2013 Mar 02
40021002008	226 ks	2013 Mar 05
40021002010[a]	16 ks	2013 Mar 09
40021003002[a]	13 ks	2013 May 28
40021003003	216 ks	2013 May 28
40021011002	246 ks	2013 Oct 30
40021012002	239 ks	2013 Nov 27
40021015002	86 ks	2013 Dec 21
40021015003	160 ks	2013 Dec 23
Total	≈2.4 Ms	

Note.
[a] Observations not considered here due to offsets from the desired pointing location.

≈18″ top-hat kernel to generate the underlying grayscale image in the left and center panels. This is comparable to the image that we used for the analysis in Grefenstette et al. (2014). While the band image is useful, it can contain some contamination from the strong non-thermal emission that is present in the remnant (Grefenstette et al. 2015) and is also not optimized to search for emission that is red- or blueshifted where some of the line flux may fall outside the 65–70 keV bandpass.

Instead of using the band image, we instead perform a systematic, spatially resolved spectroscopic analysis by dividing the remnant into an 8 × 8 grid of regions (Figure 2). Each grid box is a square with 45″ sides. The grid is centered by eye on the spatial distribution of the ^{44}Ti ejecta. The right panel in Figure 2 shows the exposure maps computed at 68 keV (this accounts for the energy-dependent vignetting) and combined in the same way as the 65–70 keV band image. It demonstrates that the exposure is relatively uniform across the grid, only dropping by ≈30% near the corners of the grid.

We use the nuproducts FTOOL to extract source spectra and generate ancillary response files (ARFs), which describe the effective area of the optics, as well as response matrix files (RMFs), which describe the response of the detectors. We generate simulated background spectra using nuskybgd (Wik et al. 2014) following the procedure described in Grefenstette et al. (2014). This results in 22 sets of data files (11 epochs × 2 telescopes) for each region. The ARF and RMF files computed by nuproducts account for the variations in the effective exposure due to vignetting described above.

We integrate over all 11 epochs by using the addspec FTOOL, setting bexpscale = 1 when calling addspec to prevent overflowing the exposure keyword. This results in two sets of source, background, ARF, and RMF files (one for FPMA and one for FPMB) for each region.

Since the ^{44}Ti emission is extended (with a spatial distribution that we do not know a priori), we have to make a decision on how to normalize the ARF.

For the spectral analysis of point sources, nuproducts adjusts the normalization of the ARF (and thus the measured flux) to account for the fraction of the PSF that falls outside the source region. This "PSF correction" is not performed when observing extended sources because the correction assumes that the extraction region is precisely centered on the point source. Here the source flux is smeared out over the source extraction region, making an accurate PSF correction impossible. Instead we opt to simply apply no PSF correction to the ARF as the most conservative approach. We address the impact of this on the interpretation of the measured flux below.

2.3. Spectral Fitting

We performed spectral fitting using XSPEC (Arnaud 1996) using the cstat statistic for the model fitting. In general, the observed (source+background) spectra satisfy the requirement that each bin contains at least one count, so we do not arbitrarily rebin the spectra before fitting. We simultaneously fit the spectra for each telescope, allowing a standard cross-normalization constant to account for variations in the overall effective area between the two telescopes.

The broadband hard X-ray spectrum of Cas A is dominated by thermal emission in the interior of the remnant along with a non-thermal tail throughout the remnant (e.g., Grefenstette et al. 2015). The non-thermal tail varies spatially across the remnant in both flux and spectral shape, so we fit each box with the srcut spectral model. We keep the radio spectral index fixed to 0.77 (which is the radio spectral index integrated over the remnant, Baars et al. 1977) and then fit for the break frequency and the normalization of the continuum. In the interior of Cas A, the data also require a thermal component, which we model using a simple bremss component. This thermal continuum can contribute significantly up to ∼15 keV. We mask the spectrum over the Fe K line features in the
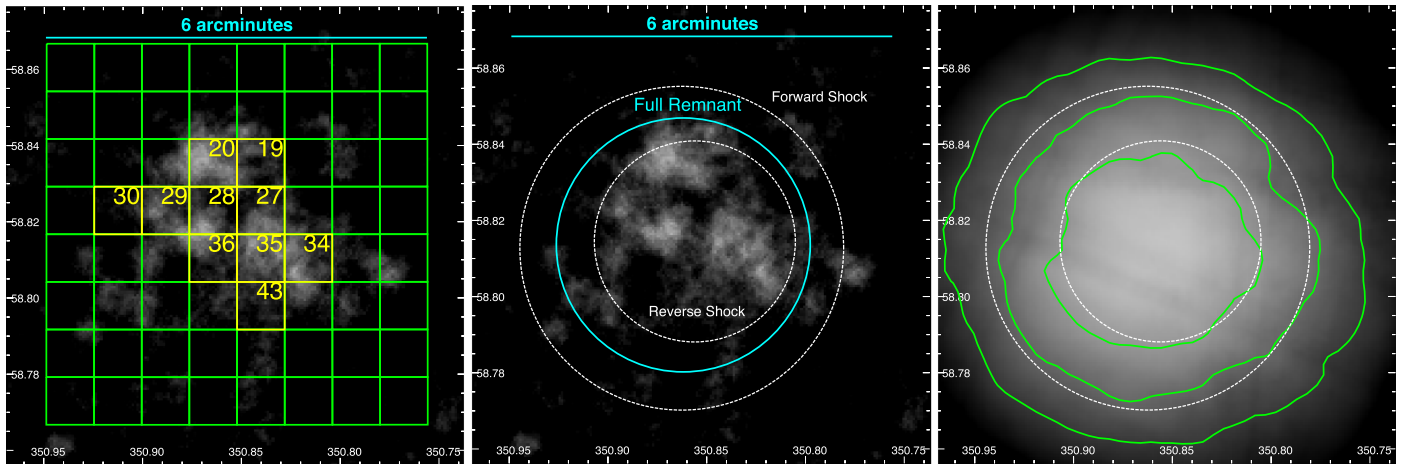
Figure 2. (Left) The 65–70 keV background-subtracted *NuSTAR* image along with the regions used for spectral analysis. The data have been smoothed with a 7-pixel (~18″) "top-hat" kernel for visual presentation. The green grid shows the regions used for spectral analysis with box 0 at top right and the box number increasing to the east (left). Box 8 is one row below box 0, Box 16 two rows below Box 0, and so on. The location of the grid was chosen to cover the ^{44}Ti evenly. Yellow boxes with associated region numbers indicate where ^{44}Ti has been detected in this analysis (see text for details). (Center) The same data, but showing the region used for the integrated ^{44}Ti flux estimate, which has a radius of 120″ and is centered on the remnant. This region is the same as used in Grefenstette et al. (2014). The locations of the forward and reverse shocks as measured by *Chandra* (Gotthelf et al. 2001) are shown by the white dashed circles. (Right) The combined exposure map computed at 68 keV after integrating over all epochs and combining both telescopes is shown by the grayscale image with a linear stretch. The green contours show the location where the exposure has dropped to 90%, 80%, and 70% of the maximum exposure, moving outward from the center.

Table 2
Results of *NuSTAR* Fits

			bremss		srcut, $\alpha = 0.77$		Gaussian		
ID	R.A.	Decl.	kT (keV)	Norm. (10^{-3})	Break (10^{17} Hz)	Norm.[a]	Centroid (keV)	1σ Width (keV)	Flux[b]
19	350.8401	58.8355	2.34 ± 0.06	7.3 ± 0.3	2.07 ± 0.09	90.9 ± 6.5	67.35 ± 0.29	<0.3	8.8 ± 2.8
20a	350.8643	58.8355	$2.14^{+0.15}_{-0.06}$	8.3 ± 0.3	$2.1^{+5.7}_{-0.1}$	65^{+5}_{-20}	67.15 ± 0.2	<0.3	12.3 ± 4.9
20b[c]	…	…	…	…	…	…	69.5 ± 0.6	$0.9^{+0.6}_{-0.4}$	$17.2^{+8.6}_{-7.4}$
27	350.8401	58.8230	2.26 ± 0.09	8.9 ± 0.3	2.8 ± 0.3	60 ± 10	66.6 ± 0.3	$0.61^{+0.4}_{-0.25}$	$11.3^{+4.6}_{-3.8}$
28	350.8643	58.8230	2.1 ± 0.1	8.2 ± 0.4	2.7 ± 0.2	56.5 ± 8	67.6 ± 0.5	<0.92	7.8 ± 5.0
29	350.8884	58.8230	2.1 ± 0.2	6 ± 0.3	$2.37^{+0.25}_{-0.48}$	37^{+14}_{-5}	$67.8^{+0.4}_{-0.9}$	0.7 ± 0.3	12.5 ± 5.5
30[c]	350.9125	58.8230	2.3 ± 0.1	6.8 ± 0.3	$3.3^{+0.5}_{-0.8}$	16^{+9}_{-3}	67.8 ± 0.6	$0.73^{+0.4}_{-0.6}$	10.6 ± 5.5
34	350.8160	58.8105	2.5 ± 0.1	7.1 ± 0.3	3.5 ± 0.2	82 ± 5	66.8 ± 0.2	<0.6	$6.4^{+4.1}_{-2.5}$
35	350.8401	58.8105	2.4 ± 0.1	7 ± 0.3	3.5 ± 0.4	46^{+9}_{-4}	67.4 ± 0.3	0.64 ± 0.3	14.4 ± 4.5
36	350.8643	58.8105	2.2 ± 0.1	7.4 ± 0.3	3.6 ± 0.2	48 ± 4	67.6 ± 0.3	0.43 ± 0.3	9.6 ± 4
43	350.8401	58.7980	2.13 ± 0.1	5.9 ± 0.1	2.72[d]	51[d]	67.1 ± 0.2	<0.34	$7.3^{+1.9}_{-3.2}$

Notes.
[a] Flux at 1 GHz in Jy.
[b] 10^{-7} photons cm^{-2} s^{-1}.
[c] Only fit with a single Gaussian line.
[d] Not well constrained.

5–7 keV band in the *NuSTAR* spectrum. This results in a fit range of 3–4.5 keV and 8.5–79 keV.

To model the ^{44}Ti decay lines we include two `Gauss` components with the line widths and fluxes tied together and require that both lines have the same observed Doppler shift. The *NuSTAR* optics have an absorption edge at ~78.4 keV (Madsen et al. 2015), so the 78.32 keV decay line is visible only when the material is stationary or redshifted. Where the 67.87 keV line is blueshifted we fit with only a single `Gaussian` component rather than the two components tied together. To determine whether the line is detected we compare the cash fit statistic with and without the ^{44}Ti lines and require that the change in fit statistic is >9.0 to declare the ^{44}Ti emission to be consistent with the data. We then use the `error` command to generate 90% and 1σ confidence regions

for the line centroid, Gaussian width, and line flux. Unless otherwise stated, all uncertainties quoted in the text are 90% error estimates.

Overall, 10 of the 64 regions satisfied our detection conditions (the fit parameters are given in Table 2).

In most of these cases the measured Gaussian 1σ widths of the lines are consistent with the energy resolution of the detectors (≈0.6 keV FWHM at 68 keV, Harrison et al. 2013). This implies that the ejecta within each 45″ region samples ^{44}Ti ejecta traveling in roughly the same direction or having a spread in velocities below the ability of *NuSTAR* to detect (i.e., the top panel in Figure 3).

The one exception is region 20 (Figure 3, bottom panel), which contains line emission clearly broadened beyond the instrument response. In this case we added a second line and
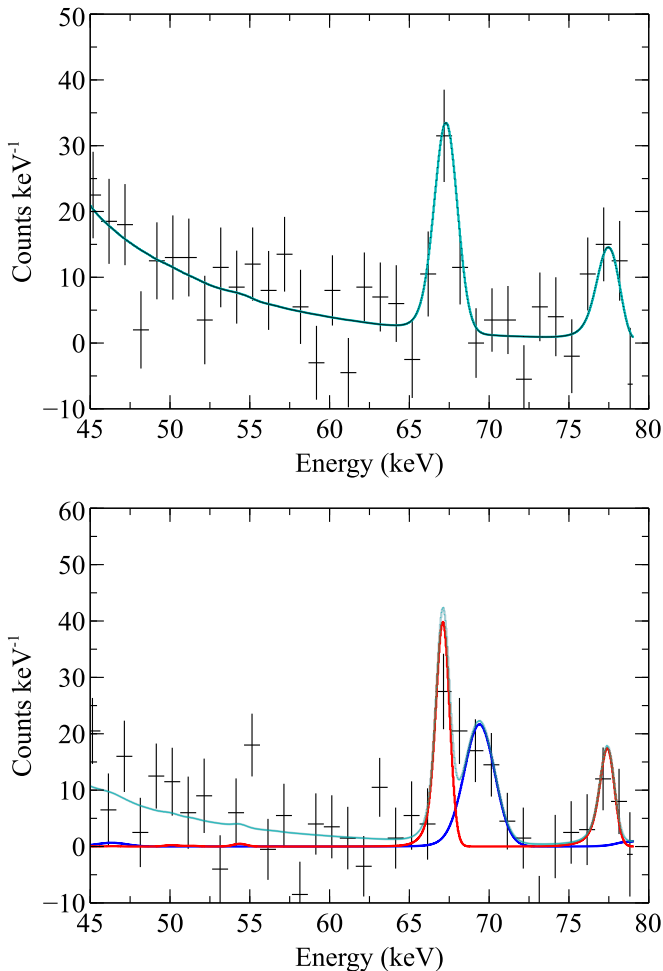
Figure 3. Spectral fits to two of the spectral regions. The data (black) are shown with 1σ error bars along with the best-fit line+continuum model (cyan). The data for the two telescopes are combined and rebinned for plotting purposes, while the models are shown unbinned. Top: region 35, which has a marginally broadened pair of ^{44}Ti lines. Bottom: region 20, showing the narrow redshifted component (for which both the 68 and 78 keV lines are observed) and the broad blueshifted component (for which only the 68 keV line is in the *NuSTAR* bandpass).

achieved an improved fit to the data, resulting in one red-redshifted component (20a) and a broad (~1 keV Gaussian width) blueshifted component (20b).

2.4. Systematic Errors

Systematic errors in the calibration of detector gain could influence the measured Doppler shift of the lines. The systematic uncertainties for *NuSTAR* are roughly 2×10^{-4} in gain and 40 eV in offset (Madsen et al. 2015). At 67.86 keV, the gain uncertainty yields a systematic error of 13 eV, or 60 km s^{-1}, while the offset uncertainty of 40 eV offset results in a systematic uncertainty in velocity of 180 km s^{-1}. Both of these effects are significantly smaller than the statistical errors, so we neglect them below.

"Look-back" effects can change the apparent bulk location of the ejecta. This is entirely an effect of the difference in light travel time between blueshifted and redshifted ejecta, where the redshifted ejecta are "younger" than the blueshifted ejecta. For unresolved sources, this can cause spherically symmetric sources to appear redshifted, especially for the gamma-ray lines from rapidly expanding supernovae (e.g., Chan &

Lingenfelter 1988). For Cas A, each region represents the integration over the line-of-sight distribution of the ejecta in the remnant. We can estimate the difference in flux due to look-back effects for ejecta. The maximum observed redshifted line had a centroid of 67.13 keV (or 1% c). This produces a 1 lt-yr line-of-sight offset per 100 yr. For a symmetric distribution of ejecta 340 yr after the explosion, the difference in apparent age between the front and rear extreme ejecta is 6.84 yr. For an e-folding time of 86.54 yr, this results in a difference in observed flux due to look-back effects of only ~8%. We conclude that look-back effects do not significantly affect our results.

3. RESULTS

3.1. The Three-dimensional Distribution of ^{44}Ti in Cas A

We can combine the distance from the center of expansion of the remnant and the observed Doppler shift of the ejecta to determine the 3D velocity of each ejecta knot. We measure the projected offsets in the plane of the sky from the center of expansion of the remnant (α(J2000) = 23^{h}23^{m}27$\overset{s}{.}$77 ± 0$\overset{s}{.}$05, δ(J2000) = 58°48′49$\overset{''}{.}$4 ± 0$\overset{''}{.}$4, Thorstensen et al. 2001). If we assume the material is freely expanding, then the observed velocity is proportional to the distance from the center of expansion of the remnant. DeLaney et al. (2010) found a proportionality constant for undecelerated ejecta of 0$\overset{''}{.}$022 per km s^{-1}. However, if a knot of ^{44}Ti ejecta has encountered the reverse shock, then the knot will be decelerated by some amount that will depend on the density of the knot and the local speed of the reverse shock at the time of the encounter. For simplicity, we will adopt the undecelerated proportionality constant for undecelerated ejecta for all of the ^{44}Ti knots because this is the most conservative projection into 3D.

Using this proportionality we can convert between observed offsets (in arcsec) and velocity (in km s^{-1}). Figure 4 shows the projected distance in the plane of the sky for each region and the measured velocity along the line of sight, together with a fiducial reverse shock radius of 95″, while Figure 5 and its associated animation show a proper 3D representation of the data.

Nearly all the ^{44}Ti ejecta are seen traveling away from the observer. However, unlike in SN1987A, where the ^{44}Ti ejecta appear to be traveling in the same direction with the same velocity (Boggs et al. 2015), here we see that the ejecta are expelled into a large solid angle. We also see ejecta that are traveling at different speeds in roughly the same direction. There is also evidence for high-velocity ^{44}Ti ejecta that have passed beyond the reverse shock (Figure 6). However, one of these knots is region 20b, which we cannot indisputably identify as a single coherent feature because it is broadened along the line of sight. Even so, there is clearly significantly blueshifted emission in this region, so there must be some ^{44}Ti ejecta that have been ejected beyond the reverse shock radius. The fact that these ejecta are beyond the reverse shock implies that our assumption that these ejecta are freely expanding is probably incorrect since they should have been decelerated as they traversed the reverse shock. However, the amount of deceleration the ejecta experience depends on the density of the ejecta, and we have no way of measuring the density of the ^{44}Ti ejecta knots. We therefore consider the positions along the line of sight to be lower limits for these data.
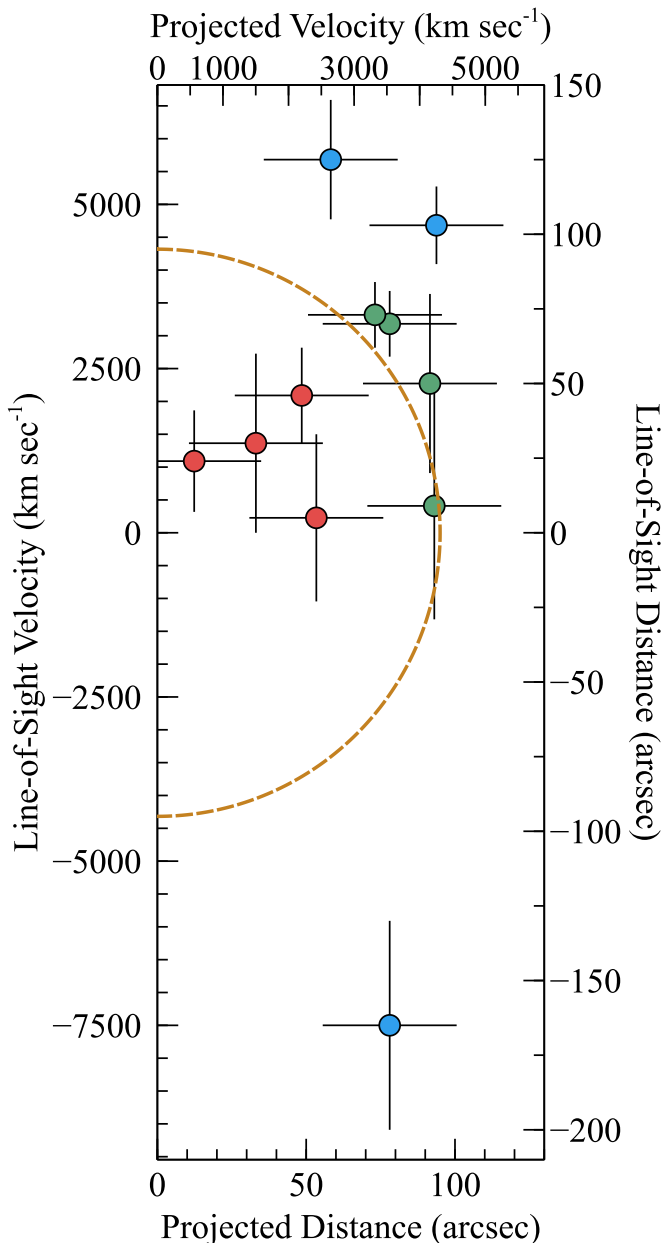
Figure 4. The measured projected distance (lower *X*-axis) and the measured velocity along the line of sight (left *Y*-axis) along with 1σ error bars. The regions that are more than 1σ interior to the reverse shock (here assumed to be a sphere with a radius of $95''$ and represented by the dashed gold curve) are colored red, the regions that are near the shock radius are colored green, while the regions more than 1σ exterior to the reverse shock are colored blue. The secondary axes give the conversion to a velocity and distance assuming a proportionality constant of $0\rlap{.}''022$ per km s^{-1} (see text for details).

3.2. The Total Mass of ^{44}Ti in Cas A Measured by NuSTAR

Simply combining the fluxes from the detected regions in Table 2 does not result in a good estimate of the total flux measured by *NuSTAR*.

As described above, for point sources a PSF correction is applied to account for the fraction of the *NuSTAR* PSF that falls outside the extraction radius. For extended sources it's not possible to apply an accurate PSF correction (and thus correctly normalize the flux) when combining neighboring regions because a region may contribute flux to its neighbors and correcting for this "loss" will overcorrect the flux.

This can be avoided by simply integrating over a larger region that covers all of the ^{44}Ti emission. Here we compute the total flux by integrating over a circular extraction region with a radius of $120''$ centered on the remnant (Figure 2, center panel). The standard behavior of `nuproducts` when producing extended ARFs is to assume that the spatial distribution of the counts for an extended source is described by the observed distribution of counts over a given energy range (i.e., that the spatial distribution of low-energy counts is the same as the distribution of high-energy counts). Here, since the source is background-dominated and since the ^{44}Ti emission does not follow any other energy band where the images are source-dominated, we instead use the `flatflagarf` keyword to produce the ARFs. This explicitly assumes the prior of a "spatially flat" distribution of source flux across the $120''$ source region. We note that this option was not available for the previous analysis.

We fit the data with a power-law continuum and a single Gaussian line (fitting over the 10–72 keV band), and a power-law continuum with two Gaussian lines with the Doppler shift of the lines, the line width, and line flux tied together (fitting over the 10–80 keV band), though the choice of model does significantly affect our results (Table 4).

We find a 68 keV line flux that is slightly higher than we previously reported ((1.84 ± 0.25) $\times 10^{-5}$ photons cm^{-2} s^{-1} compared with (1.53 ± 0.31) $\times 10^{-5}$ photons cm^{-2} s^{-1}), though the line centroid(s) and line width(s) are both consistent with our previous results. The change in flux likely arises from the improvements in the generation of the ARF (we consider the new method to be superior). Taking a distance of 3.4 kpc, an explosion date of 1671, and an average epoch of the observations of 2013 gives a total initial mass of ^{44}Ti of (1.54 ± 0.21) $\times 10^{-4}$ $M_\odot$ (compared with our previous value of (1.25 ± 0.30) $\times 10^{-4}$ $M_\odot$).

3.3. Flux Upper Limits

In regions where we do not detect ^{44}Ti emission we instead define the upper limit to be "the flux at which 50% of the time we would have detected the ^{44}Ti." We determine this by repeatedly simulating the source and background spectra using a power-law continuum (fit to the observed data between 20 and 60 keV) and inserting a single narrow Gaussian line at 67.87 keV at a given flux level. The synthetic spectrum is then fit over the 20–75 keV bandpass to see if the Gaussian component is detected as described above.

We produce 1000 simulations for each flux level using `fakeit` in XSPEC and determine how many of the simulations resulted in the detection of the line. We declare the flux level at which 50% of the simulations produce detections to be the upper limit. The upper limits vary spatially over the remnant (Figure 7) due to the vignetting of the *NuSTAR* optics (i.e., the varying exposure as seen in Figure 2, right panel) and the fact that the pointing strategy was optimized to cover the interior of the remnant with a uniform response.

4. DISCUSSION

4.1. Understanding the Relation Between Ni/Fe and Ti

Comparing the distributions of ^{44}Ti and ^{56}Ni is vital to understanding the physical conditions and kinematics of the innermost region of the supernova explosion. Most of the
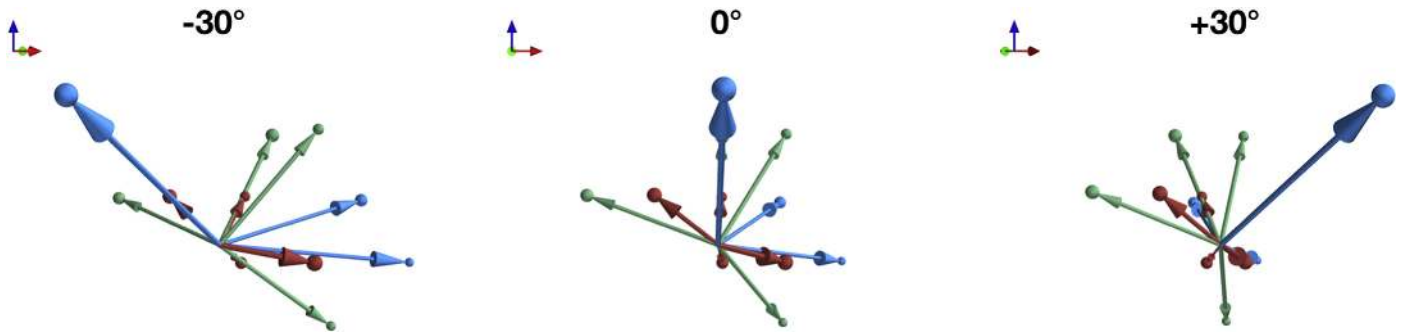
Figure 5. The 3D distribution of the ^{44}Ti ejecta. The unit vectors are north (blue), west (red), and along the observer's line of sight (green). The data vectors have an origin at the center of expansion of the remnant. The color coding is the same as for Figure 4. The center frame shows the remnant as seen by the observer, while the right/left frames have been rotated $+/-30°$ clockwise around north (blue) axis.

(An animation of this figure is available.)
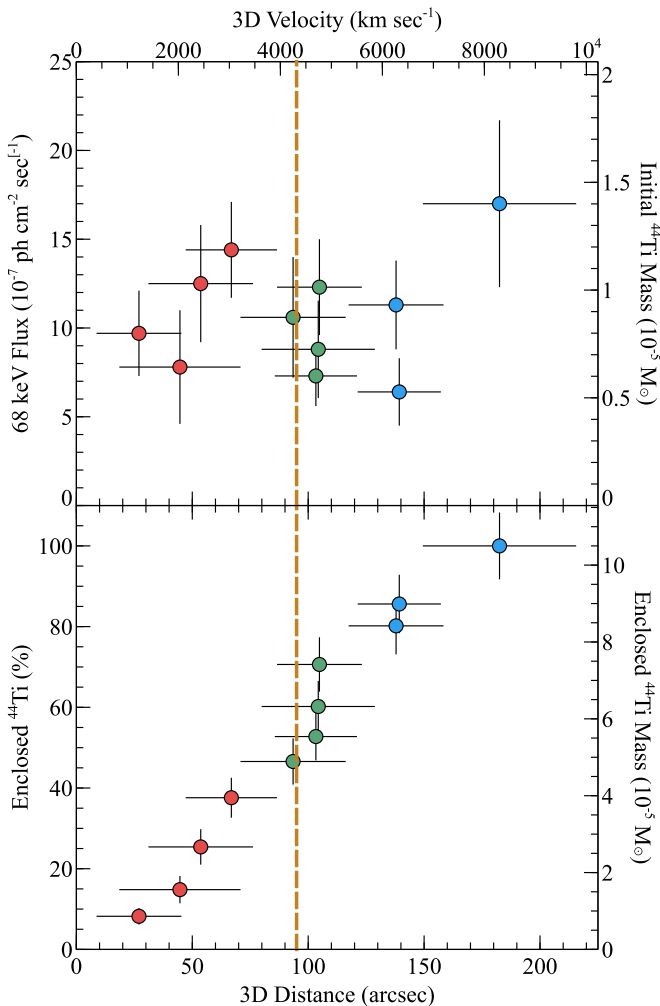
Figure 6. (Top) The flux in the 68 keV line (Y-axis) for each region is plotted against the 3D space velocity of each region (X-axis). The secondary Y-axis (right) shows the inferred initial mass of ^{44}Ti for each region assuming the distance and age of the remnant given in the text. (Bottom) The enclosed flux/mass fraction as a function of radius. Roughly 40% of the ^{44}Ti is clearly interior to the reverse shock, while 40% of the mass is at or near the reverse shock radius, leaving roughly 20% of the mass clearly exterior to the reverse shock. The color coding is the same as for Figure 4.

iron should result from the decay of ^{56}Ni, so comparing the distributions of ^{44}Ti and iron yields information on the initial distributions of nickel-rich ejecta and titanium-rich ejecta from the supernova explosion.

^{44}Ti is produced in a variety of nuclear processes, though the dominant process depends on the nature of the explosion (thermonuclear versus core collapse) and the structure of the star.

For thermonuclear supernovae, much of the ^{44}Ti is formed in the burning of the He shell or the C/O core. If the density and temperature are sufficiently low (temperatures <2–3×10^9 K and densities $<10^6$ g cm^{-3}), the material does not burn all the way to ^{56}Ni. Instead, the explosion produces ^{40}Ca, ^{44}Ti, and ^{48}Cr (Holcomb et al. 2013). In these conditions, ^{44}Ti can be produced in regions where very little or no ^{56}Ni is synthesized.

In contrast, for core-collapse supernovae like Cas A, the dominant ^{44}Ti production occurs when the shock passes through the innermost silicon layer. The densities and temperatures are typically higher than those found in the ^{44}Ti sites for thermonuclear supernovae, with peak temperatures $>4 \times 10^9$ K and densities $>10^6$ g cm^{-3} (Magkotsios et al. 2010).

The burning of silicon proceeds through photodisintegration when the rearrangement of the nuclei produces clusters of nuclei. This drives the material into nuclear statistical equilibrium, when the composition is determined by a balance between forward and reverse nuclear reaction rates. Depending upon the exact peak temperatures (and densities at these peak temperatures), Magkotsios et al. (2010) identified six regions where different processes and reactions (e.g., different quasi-equilibrium clusters and different nuclear statistical equilibrium freezeout conditions) dictate the final nucleosynthetic yields. These conditions of higher density/temperature mean that, in nearly all cases for core-collapse supernovae, at least some ^{56}Ni is produced when ^{44}Ti is produced. There are, however, scenarios in which the ^{56}Ni/^{44}Ti ratio can fall to ~100 and others where it is very high ($>10^8$). Measuring this ratio (or the Fe/Ti ratio as a proxy) and its spatial variations can provide detailed clues to the nature of the explosion.

4.1.1. Comparison of ^{44}Ti and ^{56}Ni Ejecta in 3D

Figure 8 shows the comparison of the *NuSTAR* ^{44}Ti data and the Fe K emission observed by *Chandra*. The latter data are taken from DeLaney et al. (2010), and because the iron is visible in the X-rays only after it has encountered the reverse shock we adopt the value derived by those authors to convert the line-of-sight velocity to distance of $0\farcs032$ per km s^{-1}, which is appropriate for the decelerated, reverse-shocked material.
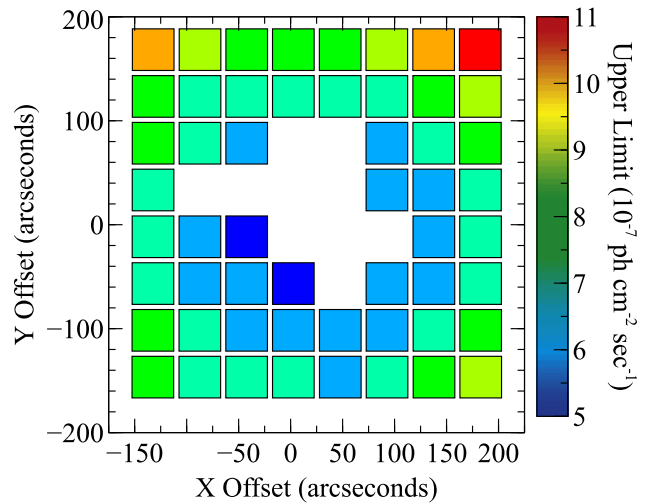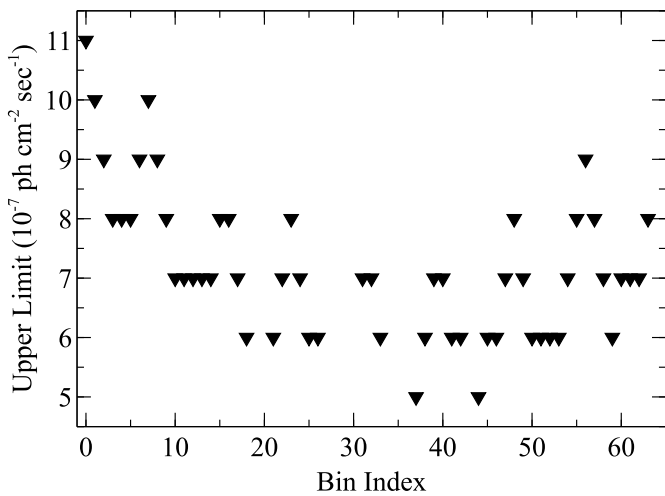
Figure 7. The upper limits for each region where the ^{44}Ti is not detected (left) and the spatial distribution of the upper limits (right). Regions where the ^{44}Ti is detected are intentionally left blank. See the text for details.
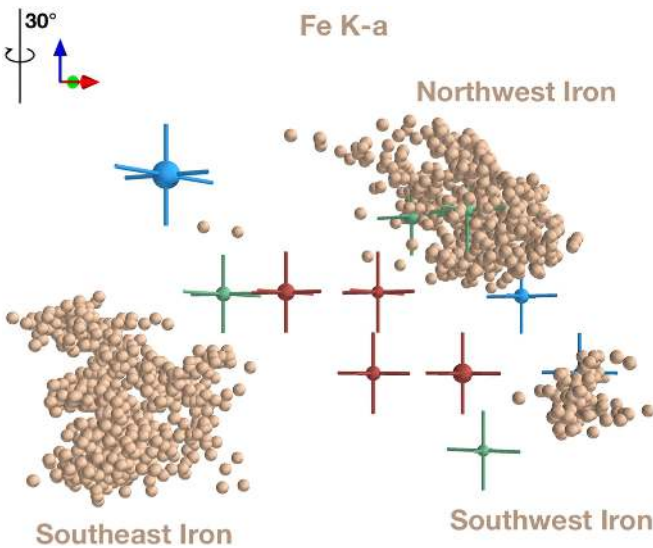
Figure 8. A 3D comparison of the ^{44}Ti ejecta observed by *NuSTAR* and the iron emission observed by *Chandra*. The ^{44}Ti data points (here shown with 1σ error bars on all three dimensions) have the same color coding as in Figure 5 and are shown against the Fe K data (gray-orange spheres) from *Chandra* (DeLaney et al. 2010). The scene has been rotated by 30° counterclockwise around the blue (north) axis. The green and blue data points (indicating that the ^{44}Ti ejecta is near or beyond the reverse shock) toward the northwest and southwest iron regions are consistent with the iron and titanium being co-located. Meanwhile, the blue data point to the top left (region 20b, projected toward the observer along the line of sight) is exterior to the reverse shock but lacks any iron counterpart. The red data points are interior to the reverse shock and may represent regions where there is diffuse, cold iron that has not yet been re-energized by the reverse shock and may be visible in the infrared.

(An animation of this figure is available.)

In nearly all cases where we see ^{44}Ti ejecta at or beyond the reverse shock (the green and blue data points in Figure 8) we also see emission from shocked iron (e.g., the regions labeled northwest and southwest Iron). The one exception to this is the blueshifted region 20b, which does have any obvious analog in the 3D distribution of shocked iron.

However, as we noted above, the line associated with region 20b is Doppler-broadened beyond the nominal energy resolution of the detectors. This implies that the PSF of *NuSTAR* is blending together several knots (or a shell) of ^{44}Ti ejecta rather

than a resolving a single knot. In this case our conversion from the Doppler velocity to a 3D position may not be correct.

There is also some evidence for a trace amount of iron in the northern shell that is stationary with respect to the center of expansion of the remnant or slightly blueshifted toward the observer. It may be the case that there is a tenuous amount of iron that would be associated with region 20b but is too faint to observed when seen in projection against the (brighter) redshifted iron (i.e., the region labeled northwest Iron in Figure 8).

We remind the reader that we need to be careful when we interpret the observed distribution of iron. First, we only observe the iron that has been shock-heated (i.e., it has passed through the reverse shock), so X-ray measurements provide a partial observation of the iron produced in the supernova. Second, estimates of the iron mass based on X-ray measurements depend upon the excitation states of the iron and so will be affected by deviations from coronal equilibrium. Since the observed X-ray flux is proportional to the product of the iron mass and electron density, highly clumped material can also produce higher X-ray flux for the same iron mass than smoothly distributed material. Finally, if iron is present in the star and the circumstellar medium, the ejecta will contain "swept-up" iron that cannot be distinguished from the iron synthesized in the explosion.

We can avoid the ambiguities in the "swept-up" iron versus iron synthesized in the explosion if we consider only iron that was producing in the explosion. A subset of the *Chandra* Fe K-emitting knots contain "pure" iron; that is, the knots are characterized by a lack of associated silicon emission (Hwang & Laming 2003, 2012). The lack of observed emission from lighter elements suggests that these regions are associated with α-rich freezeout during the explosive nucleosynthesis (Hwang & Laming 2012) rather than incomplete silicon burning. We can thus attempt to quantify the relative production rates of ^{44}Ti and iron by comparing the distribution of ^{44}Ti observed by *NuSTAR* with the distribution of pure iron observed by *Chandra* (Figure 9).

4.1.2. Beyond the Reverse Shock

For the ejecta beyond the reverse shock, there is clearly some variation that produces a large yield of ^{44}Ti in the northwest
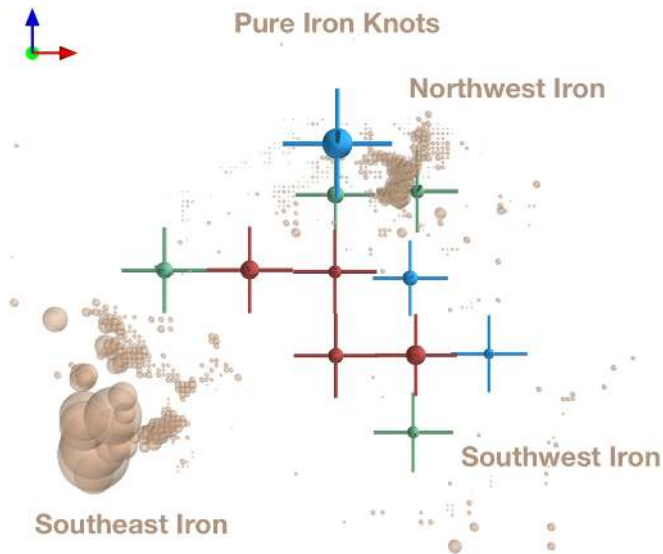
Figure 9. A comparison of the 2D "pure" iron map from Hwang & Laming (2012) and the ^{44}Ti ejecta. The data and error bars are the same as those shown as vectors in the middle panel of Figure 5 and are here shown shown face-on as seen by the observer. The gray-orange spheres are the "pure" iron ejecta and are scaled by the ejecta mass for each data point. These pure iron regions we expect to be associated with α-rich freezeout and therefore also associated with the ^{44}Ti ejecta. As for the total Fe K emission shown in Figure 8, there is pure iron in regions both with and without ^{44}Ti ejecta. The northwest, southwest, and southeast regions of iron are labeled for clarity. There is little, if any, pure ejecta in the southwest, where we otherwise find a good correlation between Fe K emission and the ^{44}Ti ejecta.

and southwest while suppressing the ^{44}Ti in the southeast. This is clear when comparing the ^{44}Ti distribution to both the Fe K 3D distribution (Figure 8) and the pure iron distribution (Figure 9).

In the northwest we integrate over the *NuSTAR* regions 19, 20a, and 27 to recover a 68 keV line flux of 32.4×10^{-7} photons cm^{-2} s^{-1}, corresponding to an initial mass of ^{44}Ti of $2.7 \times 10^{-5} M_\odot$. We similarly integrate over the regions in the *Chandra* data that are at least $30''$ north from the center of the remnant and to the west of it and find a pure iron mass of 0.014 $M_\odot$. This gives an Fe/Ti ratio of roughly 500.

We contrast this with the region of iron in the southeast of the remnant. Integrating over all knots of pure iron ejecta from *Chandra* that are south and east of the center of the remnant, we find 0.018 $M_\odot$ of pure iron but no detectable ^{44}Ti ejecta in the *NuSTAR* data. For the regions that overlap with the southeast pure iron emission the upper limits on the 68 keV flux correspond to lower limits on the Fe/Ti ratio of ~1000, or roughly twice the Fe/Ti ratio in the northwest region. The total Fe mass in the southeast region far exceeds that of the pure iron ejecta, and certainly some (or most) of this ejecta must have been synthesized in the explosion (i.e., via incomplete silicon burning, which would leave behind lighter elements to be observed), implying that the *total* Fe/Ti ratio must be $\gg 1000$ in this region.

The difference in the yield of ^{44}Ti may be a tracer of a change in the peak density of the innermost ejecta during nucleosynthesis. The yield of ^{56}Ni (and therefore pure iron) is relatively insensitive to changes in density (and, indeed, we find a comparable mass of pure iron in the northwest and southeast); the yield of ^{44}Ti can depend sensitively on the density (e.g., Magkotsios et al. 2010, 2011). The drop by at least a factor two in the ^{44}Ti yield between the northwest and

southeast regions may be evidence for large-scale asymmetry in the peak density of the innermost ejecta in these directions.

4.1.3. The Unshocked Interior

There are knots of ^{44}Ti emission interior to the Fe ejecta and the reverse shock (colored red). The combined flux from these regions is 4.5×10^{-6} photons cm^{-2} s^{-1}, which corresponds to an initial mass of roughly $4 \times 10^{-5} M_\odot$ (Figure 6) or roughly a third of the total ^{44}Ti mass in the remnant. This value is slightly underestimated because of the PSF-induced cross-talk between regions as discussed above, but is clear evidence for a significant fraction of ^{44}Ti mass residing in the interior of the remnant.

Hwang & Laming (2012) predict 0.18–0.3 $M_\odot$ of unshocked ejecta in the interior of the remnant (roughly 10% of the total ejecta mass), though it is not clear what fraction of this ejecta should be iron. If we make the assumption that the Fe/Ti ratio of ~500 as we found in the northwest, then we estimate an unshocked mass of pure iron of ~0.02 $M_\odot$ in the interior of the remnant. However, the uncertainties on this number are large; as we have seen in the exterior of the remnant there are large variations in the Fe/Ti ratio that are driven by changes in peak temperature and pressure of the innermost ejecta.

If ^{56}Ni was produced in these regions then we might expect to observe iron emission in the infrared in the interior of the remnant. Such emission has not yet been observed (Isensee et al. 2010; DeLaney et al. 2014), implying either that the interior iron ejecta are so diffuse that they cannot be detected, or that they are in a higher ionization state due to photoionization from soft X-rays from the ejecta and thus cannot be observed by *Spitzer*, or that the ejecta are not present. Deeper observations to probe for a cold, diffuse source of iron are required to further constrain the Fe/Ti ratio in the interior of the remnant.

4.2. ^{44}Ti Ejecta and Infrared/Optical Features

We can also compare the ^{44}Ti ejecta with the emission seen at optical and infrared wavelengths. This again broadly falls into two categories: ejecta that have encountered the reverse shock and ejecta that are interior to the reverse shock.

For the shocked ejecta, we can use the [Ar II] 6.99 μm 3D maps from *Spitzer* (DeLaney et al. 2010; Isensee et al. 2010). Seen in the plane of the sky, the ejecta forms the feature known as the "bright ring," while in 3D there are circular structures in the plane of the sky (labeled as the "north ring" and the "NE jet" structures, Figure 10).

We find that the ^{44}Ti ejecta appear to correlate with both the north ring and the NE jet (we recommend the movie available via the online journal for a more complete picture of these complex data). In the north ring (where we also find Fe K emission), this could have been the result of a bubble being blown in the material by the radioactive decay of clumps of ^{56}Ni (e.g., Li et al. 1993; Blondin et al. 2001). The north ring happens to be coincident with the direction of one of the light echoes from Cas A, which showed that the photosphere of the supernova to the rear/northwest direction was moving faster than along the other lines of sight to the northeast and southeast (Rest et al. 2011).

There is also emission from unshocked ejecta seen in NIR [S III] line emission (906.9 and 953.1 nm) in the interior of the remnant (Milisavljevic & Fesen 2015). These ejecta form bubble-like structures in the interior of the remnant (labeled the
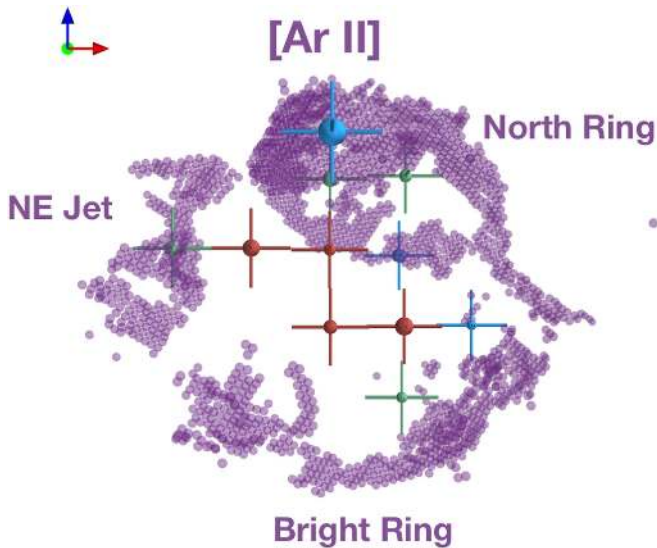
Figure 10. The 3D distribution of the observed ^{44}Ti ejecta compared with the [Ar II] emission observed by *Spitzer* (DeLaney et al. 2010). The ^{44}Ti ejecta are shown with 1σ error bars and retain the color scheme from Figure 5. The infrared data are shown in magenta along with labels to identify important features. The scene is displayed as seen by the observer, though an animation showing the full rotation of the remnant is available in the online journal. Upon rotation, the association of ^{44}Ti ejecta with features in the [Ar II] map (specifically in the "north ring" and the ring near the "NE jet") becomes clearer.

(An animation of this figure is available.)

Figure 11. The 3D distribution of the observed ^{44}Ti ejecta compared with the NIR [S III] emission (data from Milisavljevic & Fesen 2015). The ^{44}Ti ejecta are shown with 1σ error bars and retain the color scheme from Figure 5. The infrared data are shown in magenta along with lines to identify the north and south cavities. The scene is rotated by 90° counterclockwise around the north axis and shows the view from the west (the same orientation as for Figure 2 from Milisavljevic & Fesen 2015). Upon rotation, a rough association of the inner ^{44}Ti ejecta with the north cavity become clearer. We do not see any ^{44}Ti ejecta associated with the blueshifted (i.e., the lower left side in the above rendering) south cavity.

(An animation of this figure is available.)

"north" and "south" cavities in Figure 11). We find that the ^{44}Ti ejecta may be associated with the northern cavity seen in the [S III] data, though we do not see any evidence for ^{44}Ti being associated with the southern, blueshifted cavity. We expect these bubbles to be associated with the decay of ^{56}Ni and so we may be seeing variations in the resulting Fe/Ti ratio in the interior of the remnant similar to the variations that we observe beyond the reverse shock.
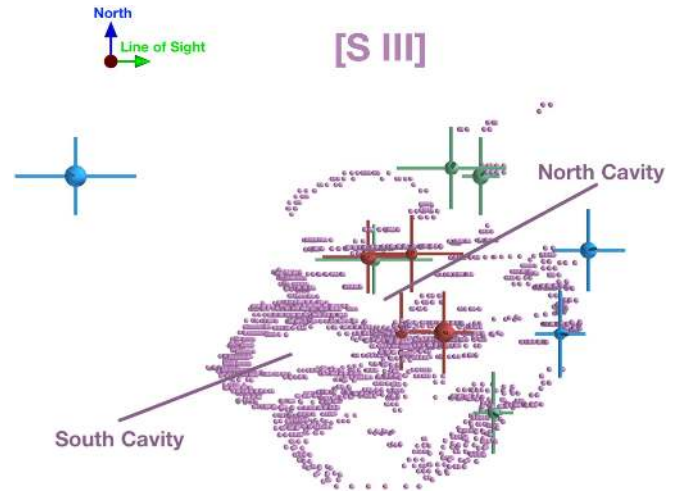
The interior unshocked ejecta is also seen in the infrared via [Si II] (34.8 μm) emission (DeLaney et al. 2010). These ejecta are apparently arranged into a "tilted thick disk" (identified in Figure 12) with a significant gap between the redshifted and blueshifted faces. We do not see any evidence for ^{44}Ti ejecta associated with the blueshifted half of the thick disk, though we do see that the redshifted ^{44}Ti ejecta are reasonably consistent with the redshifted half of the thick disk.

A future instrument with spatial resolution comparable to what is achieved by *Chandra* or *Spitzer* and spectral resolution better than *NuSTAR* will likely be required to study the relative associations of the optical/infrared and ^{44}Ti in the interior of the remnant in further detail.

4.3. ^{44}Ti Ejecta and the CCO Kick

The discovery of a point-like X-ray source (hereafter the central compact object, or CCO) in Cas A was one of the major results of the first images of Cas A taken at high spatial resolution with *Chandra* (Tananbaum 1999). The CCO is now thought to be consistent with a slowly rotating neutron star (e.g., Pavlov et al. 2000; Chakrabarty et al. 2001; Mereghetti et al. 2002) or, perhaps, a neutron star with a low surface magnetic field (e.g., Pavlov & Luna 2009).

If we accept that the CCO is a neutron star, then we can use it to study the natal kick of the neutron star (e.g., Burrows & Hayes 1996; Burrows et al. 2004; Wongwathanarat

et al. 2013). The CCO is offset from the center of expansion of the remnant by $7\rlap{.}''0 \pm 0\rlap{.}''8$ with a position angle of $169° \pm 8.4°$ in an observation made in 2004 (Fesen et al. 2006). For an explosion date of ∼1671 and a distance of 3.4 kpc, this corresponds to a velocity in the plane of the sky of ∼330 km s^{-1}. None of the major features in the remnant observed in the optical, infrared, or radio appears to match the CCO motion, though the bulk motion of the X-ray-emitting ejecta in the remnant (210 km s^{-1} east and 680 km s^{-1} north, Hwang & Laming 2012) is ∼150° from the direction of motion of the CCO.

The bulk of the ^{44}Ti, however, is traveling in the west/northwest direction away from the observer. Using the flux-weighted mean of the 3D velocities given in Table 3, we find that the average direction of motion of the ^{44}Ti ejecta has a position angle of ∼340° ± 15° (measured clockwise from celestial north in the plane of the sky) and is tilted by 58° ± 20° into the plane of the sky away from the observer (Figure 13). The angle in the plane of the sky is almost exactly opposite to the inferred direction of the CCO motion.

If we assume that the 3D distribution of the ^{44}Ti ejecta is a tracer of the 3D mass of the innermost ejecta at the time of the explosion and that the neutron star kick is related to the asymmetries in the ejecta mass distribution, then we can make a prediction about the velocity of the neutron star along the line of sight. We can then proceed assuming that there is a simple scaling relation between the total momentum of the ^{44}Ti and the momentum of the neutron star:

$$C \times \rho_{\mathrm{Ti}} = \rho_{\mathrm{NS}} \tag{1}$$

where C is some proportionality constant that is roughly the ratio of the ^{44}Ti ejecta mass to the total inner ejecta mass. Since we can directly measure the velocity components of both the
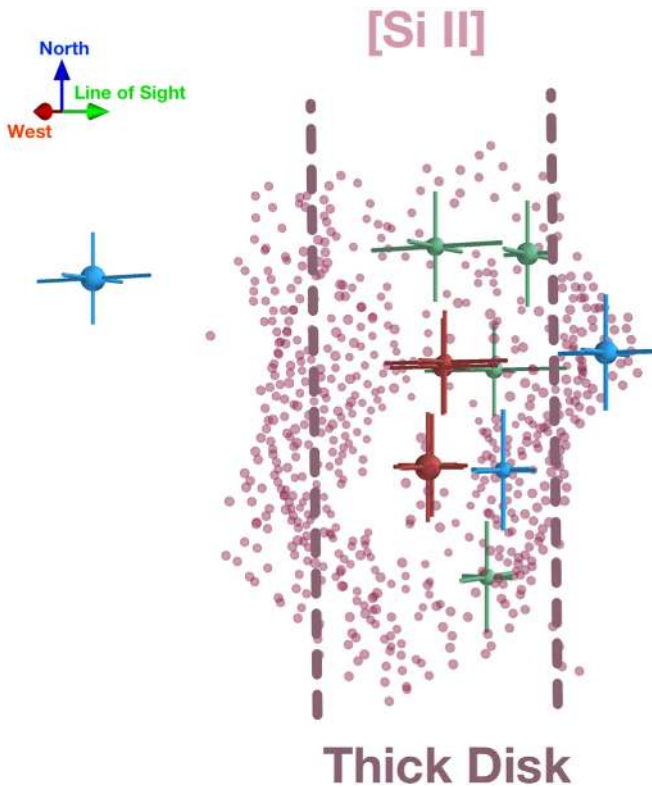
Figure 12. The 3D distribution of the observed ^{44}Ti ejecta compared with the IR [Si II] emission observed by *Spitzer* (DeLaney et al. 2010). The ^{44}Ti ejecta are shown with 1σ error bars and retain the color scheme from Figure 5. The infrared data are shown in magenta along with lines to identify the extent of the "thick disk" region. The scene is rotated by 120° counterclockwise around the north axis. Upon rotation, the association of the inner ^{44}Ti ejecta with the [Si II] map (specifically near the center of the thick disk) become clearer. We do not see any ^{44}Ti ejecta associated with the blueshifted (i.e., the left side in the above rendering) face of the thick disk.

(An animation of this figure is available.)

^{44}Ti and the neutron star in the plane of the sky, we can fold the neutron star mass into the proportionality constant itself and make the comparison:

$$\langle \boldsymbol{v}_{\mathrm{Ti}} \rangle_{\mathrm{Sky}} = C' \times \boldsymbol{v}_{\mathrm{NS,Sky}} \qquad (2)$$

where $\langle \boldsymbol{v}_{\mathrm{Ti}} \rangle_{\mathrm{Sky}}$ is the flux-weighted mean velocity of the ^{44}Ti ejecta in the plane of the sky. The ^{44}Ti has an observed velocity in the plane of the sky of 1450 ± 380 km s^{-1}, so we can compute the proportionality constant C' that will produce a velocity of the neutron star in the plane of the sky of 330 km s^{-1}. Assuming the same proportionality constant applies to the line-of-sight direction we can convert the flux-weighted average of the ^{44}Ti velocity along the line of sight (920 ± 510 km s^{-1}) into an estimate for the line-of-sight velocity of the neutron star (205 ± 125 km s^{-1}).

Unfortunately, testing this hypothesis is non-trivial, the uncertainties we quote here are large, and the physical scaling that we have performed here to convert between the ^{44}Ti momentum and the neutron star kick is likely overly simplistic. However, the fact that the ^{44}Ti ejecta are apparently moving in the direction opposite to that of the neutron star strongly suggests that the two are related. When we also consider that the bulk ejecta is recoiling in roughly the same direction as the ^{44}Ti and opposite to the direction of the neutron star (Hwang & Laming 2012) and that the light echo in this region indicates that the exploding star was moving faster than along the other lines of sight to the northeast

and southeast (Rest et al. 2011), then we start to construct a more complete picture of the explosion. If the ejecta expands rapidly (perhaps as the result of a more energetic explosion), then the density can quickly drop into a region where α-rich freezeout may occur, resulting in a high yield of ^{44}Ti.

4.4. Implications for Instabilities

One of the most important unresolved issues currently facing the supernova simulation community is whether supernova explosions can be adequately modeled in 2D (i.e., the explosion can be described by axisymmetric simulations) or whether they require 3D simulations to fully capture the relevant instabilities (see, e.g., recent reviews by Fryer et al. 2014; Janka et al. 2016). The favored interpretation for a core-collapse supernova is that neutrino heating drives shock instabilities in the collapsing star (e.g., Bethe & Wilson 1985). These instabilities give rise to large spatial structures (i.e., those that can be described by "low-mode" spherical harmonics), or bubbles, in the ejecta that carry enough momentum to revive the stalled shock and explode the star. The *NuSTAR* 2D ^{44}Ti map of Cas A strongly supports this low-mode convection model for the supernova engine (Grefenstette et al. 2014).

We have also previously argued that even the 2D images of the ^{44}Ti ejecta suggest that large-scale structures dominate the ejecta distribution rather than small turbulent eddies (i.e., features that can be described by "high-mode" spherical harmonics) or "jet"-like features that can result from the collapse of a rapidly rotating massive star like those that are present in Type Ib/Ic supernovae and/or gamma-ray bursts (e.g., Mösta et al. 2015). The generation of these large structures in 3D may be related to the standing-mode accretion shock instability (SASI), which redistributes power to lower spherical harmonics in 3D simulations while turbulence will drive power to higher order modes (Janka et al. 2016). This can also occur in Rayleigh–Taylor driven convection (e.g., Herant 1995).

The fact that we now see large, coherent structures in the 3D distribution of the ejecta is further evidence that the large spatial instabilities do not cascade down to small spatial scales in less than a dynamical timescale. This is especially true when we consider the spatial variations of the measured Fe/Ti abundance, which is nearly bipolar in structure and may be the best tracer for density asymmetries in the innermost ejecta during explosive nucleosynthesis.

5. SUMMARY

We have presented results from the 2.4 Ms *NuSTAR* campaign designed to study the ^{44}Ti ejecta in Cas A. These data provide the first opportunity to study the 3D distribution of ^{44}Ti in Cas A. The ability to spatially resolve the emission from the ^{44}Ti ejecta provides us with a new probe for studying nucleosynthesis in the supernova explosion by studying the relative spatial distributions of the ^{44}Ti-rich ejecta and the ^{56}Ni-rich ejecta.

The average momentum (i.e., the flux-weighted average of the ^{44}Ti ejecta velocities) gives a resulting vector rotated in the plane of the sky by $\sim$340° $\pm$ 15° (measured clockwise from celestial north) and tilted by 58° $\pm$ 20° into the plane of the sky away from the observer. The velocity in the plane of the sky is almost precisely opposite to the direction of the Cas A CCO. This is highly suggestive that the ^{44}Ti ejecta is tracing out the instabilities that led to the neutron star kick in Cas A. We therefore expect that the neutron star should have a significant
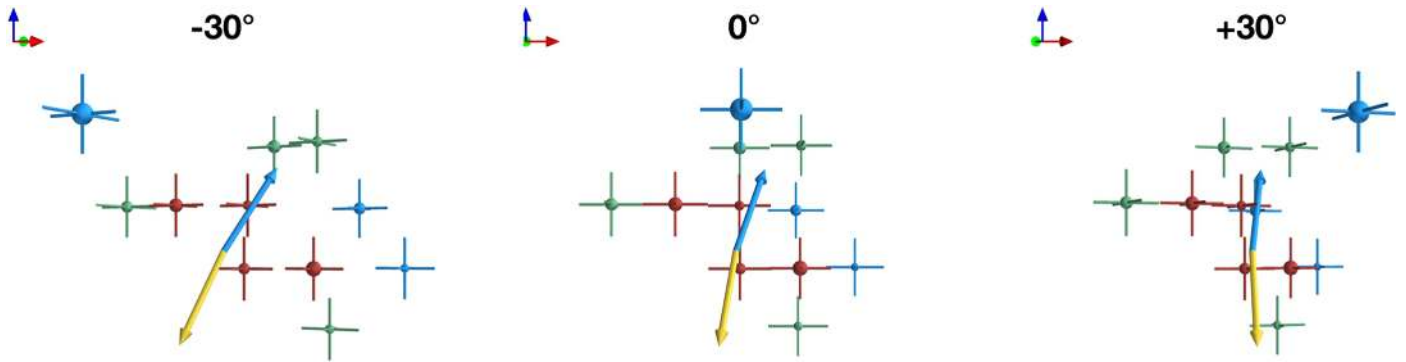
Figure 13. The 3D distribution of the observed ^{44}Ti ejecta compared with the CCO motion. The unit vectors are north (blue), west (red) and along the observer's line of sight (green). The data points show the ^{44}Ti data along with 1σ errors and have the same color scheme as in Figure 5. The blue vector shows the flux-weighted mean direction of motion of the ^{44}Ti, while the gold vector shows the direction of motion of the CCO, where the CCO is assumed to be moving opposite to the direction of the ^{44}Ti along the line of sight and at a position angle of 169° clockwise from north (see text). The center frame shows the remnant as seen by the observer, while the right/left frames have been rotated $+/-30°$ clockwise around the north (blue) axis.

(An animation of this figure is available.)

Table 3
NuSTAR 3D Data

ID	Offsets (arcsec)			Velocities (km s^{-1})		
	West[a]	North[a]	Line of Sight[b]	West	North	Line of Sight[b]
19	48 ± 22.5	78 ± 22.5	50 ± 30	2200 ± 1020	3500 ± 1020	2300 ± 1400
20a	3 ± 22.5	78 ± 22.5	70 ± 11	140 ± 1020	3500 ± 1020	3200 ± 500
20b	3 ± 22.5	78 ± 22.5	-170 ± 35	140 ± 1020	3500 ± 1020	-7500 ± 1600
27	48 ± 22.5	33 ± 22.5	125 ± 20	2200 ± 1020	1500 ± 1020	5700 ± 910
28	3 ± 22.5	33 ± 22.5	30 ± 30	120 ± 1020	1500 ± 1020	1400 ± 1400
29	-42 ± 22.5	33 ± 22.5	5 ± 28	-1900 ± 1020	1500 ± 1020	230 ± 1300
30	-87 ± 22.5	33 ± 22.5	9 ± 38	-4000 ± 1020	1500 ± 1020	410 ± 1700
34	93 ± 22.5	-12 ± 22.5	100 ± 13	4200 ± 1020	-550 ± 1020	4700 ± 590
35	47 ± 22.5	-12 ± 22.5	46 ± 16	2100 ± 1020	-550 ± 1020	2100 ± 730
36	3 ± 22.5	-12 ± 22.5	24 ± 17	140 ± 1020	-550 ± 1020	1100 ± 770
43	47 ± 22.5	-56 ± 22.5	73 ± 11	2100 ± 1020	-2500 ± 1020	3300 ± 500
Mean[c]	10.8 ± 8.0	30.4 ± 8.0	20.2 ± 11.0	490 ± 360	1380 ± 380	920 ± 510

Notes. Error bars are 1σ and include the uncertainties on the measured flux from Table 2.
[a] West and north uncertainties are the half-length of the square regions.
[b] Line-of-sight uncertainties are based on the 1σ error ranges from the line fits.
[c] Flux-weighted mean of all regions.

Table 4
NuSTAR Cas A Integrated Fits

Line Model (Fit Range)	Power-law Parameters		67.87 keV Gauss Parameters			Initial ^{44}Ti
	Γ	Norm.[a] (photons cm^{-2} s^{-1})	Centroid (keV)	Width (keV)	Flux (10^{-5} photons cm^{-2} s^{-1})	Mass ($10^{-4} M_\odot$)
Single line (10–72 keV)	3.36 ± 0.05	1.229 ± 0.015	$67.44^{+0.11}_{-0.14}$	0.68 ± 0.15	1.84 ± 0.25	1.52 ± 0.2
Two lines (10–80 keV)	3.36 ± 0.05	1.229 ± 0.015	$67.41^{+0.10}_{-0.12}$	0.69 ± 0.15	1.87 ± 0.24	1.54 ± 0.2

Notes.
[a] Flux at 1 keV.

transverse (line of sight) velocity toward the observer, though we have no observational means of testing this hypothesis.

We find ^{44}Ti ejecta interior to the reverse shock, though these ejecta cannot be definitively associated with known features observed in the optical or the infrared. The present-day flux from this ejecta implies that there is an initial mass of $\sim 4 \times 10^{-5} M_\odot$ of ^{44}Ti interior to the reverse shock. If we

assume this interior ejecta has a comparable Ni/Ti ratio to the regions exterior to the reverse shock (implying an Fe/Ti ratio of ~ 500) then we estimate that there is $0.02 M_\odot$ of "hidden" iron in the interior of Cas A, though we caution that this value is highly model-dependent.

Where we see ^{44}Ti ejecta near or exterior to the reverse shock in 3D we generally see emission from shock-heated iron,

which should mostly be descended from ^{56}Ni that is synthesized along with the ^{44}Ti in the explosion. This is true both of iron that is associated with lighter elements, which may be the result of incomplete silicon burning, as well as regions of "pure" iron that we think result from α-rich freezeout. While there is some evidence for ^{44}Ti ejecta exterior to the reverse shock where we do not observe any associated iron, we are not convinced that either the interpretation of the 3D location of the Doppler-broadened region of ^{44}Ti ejecta is correct or that the lack of observed iron implies that the iron is not present.

Conversely, we do find regions of iron emission exterior to the reverse shock where we do not see associated ^{44}Ti emission. This is true both for the iron we think is associated with incomplete silicon burning and the iron we think is associated with α-rich freezeout. The upper limits on the presence of ^{44}Ti in these exterior regions suggest that the ^{44}Ti yield must be suppressed by at least a factor of two relative to the yield of ^{56}Ni in these regions to explain the lack of observed ^{44}Ti ejecta.

REFERENCES

Ahmad, I., Greene, J., Moore, E., et al. 2006, PhRvC, 74, 065803
Arnaud, K. A. 1996, in ASP Conf. Ser. 101, Astronomical Data Analysis Software and Systems V, ed. G. H. Jacoby & J. Barnes (San Francisco, CA: ASP), 17
Baars, J. W. M., Genzel, R., Pauliny-Toth, I. I. K., & Witzel, A. 1977, A&A, 61, 99
Bethe, H. A., & Wilson, J. R. 1985, ApJ, 295, 14

Blondin, J. M., Borkowski, K. J., & Reynolds, S. P. 2001, ApJ, 557, 782
Boggs, S. E., Harrison, F. A., Miyasaka, H., et al. 2015, Sci, 348, 670
Burrows, A., & Hayes, J. 1996, PhRvL, 76, 352
Burrows, A., Ott, C. D., & Meakin, C. 2004, in Cosmic Explosions in Three Dimensions, ed. P. Hoflich, P. Kumar, & J. C. Wheeler (Cambridge: Cambridge Univ. Press), 209
Chakrabarty, D., Pivovaroff, M. J., Hernquist, L. E., Heyl, J. S., & Narayan, R. 2001, ApJ, 548, 800
Chan, K. W., & Lingenfelter, R. E. 1988, in AIP Conf. Proc. 170 (Melville, NY: AIP), 110
Chen, J., Singh, B., & Cameron, J. 2011, NDS, 112, 2357
DeLaney, T., Kassim, N. E., Rudnick, L., & Perley, R. A. 2014, ApJ, 785, 7
DeLaney, T., Rudnick, L., Stage, M. D., et al. 2010, ApJ, 725, 2038
Fesen, R. A., Hammell, M. C., Morse, J., et al. 2006, ApJ, 645, 283
Fryer, C. L., Even, W., Grefenstette, B. W., & Wong, T.-W. 2014, AIPA, 4, 041014
Gotthelf, E. V., Koralesky, B., Rudnick, L., et al. 2001, ApJL, 552, L39
Grebenev, S. A., Lutovinov, A. A., Tsygankov, S. S., & Winkler, C. 2012, Natur, 490, 373
Grefenstette, B. W., Harrison, F. A., Boggs, S. E., et al. 2014, Natur, 506, 339
Grefenstette, B. W., Reynolds, S. P., Harrison, F. A., et al. 2015, ApJ, 802, 15
Harrison, F. A., Craig, W. W., Christensen, F. E., et al. 2013, ApJ, 770, 103
Herant, M. 1995, PhR, 256, 117
Holcomb, C., Guillochon, J., De Colle, F., & Ramirez-Ruiz, E. 2013, ApJ, 771, 14
Hwang, U., & Laming, J. M. 2003, ApJ, 597, 362
Hwang, U., & Laming, J. M. 2012, ApJ, 746, 130
Isensee, K., Rudnick, L., DeLaney, T., et al. 2010, ApJ, 725, 2059
Iyudin, A. F., Diehl, R., Bloemen, H., et al. 1994, A&A, 284, L1
Janka, H. T., Melson, T., & Summa, A. 2016, ARNPS, 66, 341
Li, H., McCray, R., & Sunyaev, R. A. 1993, ApJ, 419, 824
Madsen, K. K., Harrison, F. A., Markwardt, C. B., et al. 2015, ApJS, 220, 8
Magkotsios, G., Timmes, F. X., Hungerford, A. L., et al. 2010, ApJS, 191, 66
Magkotsios, G., Timmes, F. X., & Wiescher, M. 2011, ApJ, 741, 78
Martin, P., Knödlseder, J., Vink, J., Decourchelle, A., & Renaud, M. 2009, A&A, 502, 131
Mereghetti, S., Tiengo, A., & Israel, G. L. 2002, ApJ, 569, 275
Milisavljevic, D., & Fesen, R. A. 2015, Sci, 347, 526
Mösta, P., Ott, C. D., Radice, D., et al. 2015, Natur, 528, 376
Nagataki, S., Hashimoto, M.-A., Sato, K., Yamada, S., & Mochizuki, Y. S. 1998, ApJL, 492, L45
Pavlov, G. G., & Luna, G. J. M. 2009, ApJ, 703, 910
Pavlov, G. G., Zavlin, V. E., Aschenbach, B., Trümper, J., & Sanwal, D. 2000, ApJL, 531, L53
Ramachandran, P., & Varoquaux, G. 2011, CSE, 13, 40
Reed, J. E., Hester, J. J., Fabian, A. C., & Winkler, P. F. 1995, ApJ, 440, 706
Renaud, M., Vink, J., Decourchelle, A., et al. 2006, ApJL, 647, L41
Rest, A., Foley, R. J., Sinnott, B., et al. 2011, ApJ, 732, 3
Rothschild, R. E., & Lingenfelter, R. E. 2003, ApJ, 582, 257
Siegert, T., Diehl, R., Krause, M. G. H., & Greiner, J. 2015, A&A, 579, A124
Tananbaum, H. 1999, IAUC, 7246, 1
The, L. S., Leising, M. D., Kurfess, J. D., et al. 1996, A&AS, 120, 357
Thorstensen, J. R., Fesen, R. A., & van den Bergh, S. 2001, ApJ, 122, 297
Vink, J., Laming, J. M., Kaastra, J. S., et al. 2001, ApJL, 560, L79
Wik, D. R., Hornstrup, A., Molendi, S., et al. 2014, ApJ, 792, 48
Wongwathanarat, A., Janka, H. T., & Müller, E. 2013, A&A, 552, A126
Woosley, S. E., Arnett, W. D., & Clayton, D. D. 1973, ApJS, 26, 231
Woosley, S. E., & Hoffman, R. D. 1992, ApJ, 395, 202